


Article

Enhancing Photoelectrocatalytic Efficiency of BiVO₄ Photoanodes by Crystal Orientation Control

Hongru Zhao ^{1,2}, Xinkong Wei ², Yue Pei ² and Weihua Han ^{1,2,*} ¹ Guangzhou Institute of Blue Energy, Guangzhou 510555, China; zhaohr21@lzu.edu.cn² School of Physical Science and Technology, Lanzhou University, Lanzhou 730000, China; 220220939981@lzu.edu.cn (X.W.); pyue2023@lzu.edu.cn (Y.P.)

* Correspondence: hanwh@lzu.edu.cn

Abstract: Bismuth Vanadate (BiVO₄) is a promising photoanode material due to its stability and suitable bandgap, making it effective for visible light absorption. However, its photoelectrocatalytic efficiency is often limited by the poor transport dynamics of photogenerated carriers. Recent research found that varying the atomic arrangement in crystals and Fermi levels across different crystal orientations can lead to significant differences in carrier mobility, charge recombination rates, and overall performance. In this work, we optimized the atomic arrangement by controlling the crystal growth direction to improve carrier separation efficiency using a wet chemical method. Systematic investigations revealed that the preferential [010]-oriented BiVO₄ film exhibits the highest carrier mobility and photocurrent density. Under an applied bias of 1.21 V (vs. RHE) in a 0.5 M Na₂SO₄ electrolyte, it achieved a photocurrent density of 0.2 mA cm⁻² under AM 1.5 G illumination, significantly higher than that of the [121]-oriented (0.056 mA cm⁻²) and randomly oriented films (0.11 mA cm⁻²). This study provides a deeper understanding of the role of crystal orientation in enhancing photoelectrocatalytic efficiency.

Keywords: photoelectrocatalysis; crystal facet engineering; carrier mobility; charge separation efficiency



Citation: Zhao, H.; Wei, X.; Pei, Y.; Han, W. Enhancing Photoelectrocatalytic Efficiency of BiVO₄ Photoanodes by Crystal Orientation Control. *Nanomaterials* **2024**, *14*, 1870. <https://doi.org/10.3390/nano14231870>

Academic Editor: Francis Leonard Deepak

Received: 27 October 2024

Revised: 17 November 2024

Accepted: 18 November 2024

Published: 21 November 2024



Copyright: © 2024 by the authors. Licensee MDPI, Basel, Switzerland. This article is an open access article distributed under the terms and conditions of the Creative Commons Attribution (CC BY) license (<https://creativecommons.org/licenses/by/4.0/>).

1. Introduction

Photoelectrocatalysis offers a promising solution to the global energy crisis and environmental challenges by converting solar energy into stable chemical energy stored in energy-dense molecules [1–3]. Metal oxides are ideal candidates for photoelectrocatalytic materials due to their high stability, low cost, and availability [4]. The photoelectrochemical (PEC) process involves three crucial steps: light absorption, separation and transport of photogenerated carriers, and surface redox reactions. Among these, the transport and separation of carriers often limit overall PEC efficiency [5–7]. In most metal oxides, the short diffusion length of photogenerated carriers leads to recombination before they can reach the surface, severely hindering PEC performance [8]. For instance, hematite has a light penetration depth of approximately 118 nm at 550 nm, which is significantly longer than its hole diffusion length of only 2–4 nm [9]. Similarly, BiVO₄ is limited by a hole diffusion length of less than 40 nm, which constrains its photocurrent generation [10]. Even in widely studied materials, like polycrystalline TiO₂, the solar-to-fuel conversion efficiency remains restricted due to short minority carrier diffusion lengths ranging from 10 to 100 nm [11].

Enhancing carrier diffusion length and separation efficiency is thus a critical challenge. While research has focused on increasing carrier mobility within photoelectrodes, grain boundaries and short hole diffusion lengths relative to light absorption create obstacles. Recent studies suggest that controlling crystal orientation can significantly improve carrier mobility and reduce recombination [12–14]. For example, Pan et al. demonstrated that Cu₂O films grown along the [111] orientation exhibit a carrier mobility of 15.4 cm² V⁻¹ s⁻¹,

which is significantly higher compared to films with [100] ($1.29 \text{ cm}^2 \text{ V}^{-1} \text{ s}^{-1}$) and [110] ($0.87 \text{ cm}^2 \text{ V}^{-1} \text{ s}^{-1}$) orientations [15]. Similarly, Kay et al. found that the conductivity of hematite ($\alpha\text{-Fe}_2\text{O}_3$) along the [110] orientation was four orders of magnitude higher than in the orthogonal direction [16]. These findings underscore the potential of crystal facet engineering to enhance carrier mobility and PEC activity [17–20].

BiVO_4 , with its narrow bandgap (2.4 eV), negative conduction band edge (0 V vs. RHE), earth abundance, non-toxicity, and excellent stability, has emerged as a prominent material for photoelectrocatalysis [21–24]. However, current methods to improve BiVO_4 film quality require high vacuum, high temperatures, and specialized equipment. In this work, we introduce a novel strategy for improving BiVO_4 's photoelectrocatalytic performance by controlling the crystal growth orientation of the material. This approach, which utilizes a simple wet chemical method, operates under ambient pressure, making it more cost-effective and scalable compared to conventional high-temperature or high-vacuum techniques. By tuning the growth temperature, we achieve BiVO_4 films with distinct crystal orientations, significantly enhancing the material's carrier mobility and photocurrent density.

In this study, we successfully prepared BiVO_4 films with controlled crystal growth orientations using a wet chemical method by regulating the water bath temperature. This approach allows for film growth under ambient pressure while maintaining excellent stability during PEC processes. Our results show that BiVO_4 photoanodes grown along the [010] crystal orientation achieve significantly higher carrier separation efficiency and photocurrent density compared to other orientations. Specifically, the photocurrent density of [010]-oriented BiVO_4 is 3.5 times higher than that of the [121] orientation and twice that of films with no specific orientation. Conductive atomic force microscopy (C-AFM) testing and fitting confirm that [010]-oriented BiVO_4 exhibits superior carrier mobility and diffusion length, offering an effective strategy for enhancing carrier separation efficiency in photoelectrodes.

2. Materials and Methods

2.1. Chemicals and Reagents

$\text{Bi}(\text{NO}_3)_3 \cdot 5\text{H}_2\text{O}$ (AR, 99%) and NH_4VO_3 (AR, 99%) were acquired from Aladdin Chemical Reagent Co., Ltd. (Shanghai, China). HNO_3 (AR), acetone (AR), and ethanol (AR) were purchased from Chengdu Kelong Chemical Reagent Co., Ltd. (Chengdu, China). Acetonitrile (AR) was obtained from Tianjin Damao Chemical Reagent Factory, and Fluorine-doped tin oxide (FTO) glass was purchased from Huanan Xiangcheng Technology Co., Ltd. (Shenzhen, China).

2.2. Preparation of the Samples

The synthesis of BiVO_4 films follows a solution-based method combined with controlled annealing. First, 1.21 g of $\text{Bi}(\text{NO}_3)_3 \cdot 5\text{H}_2\text{O}$ and 0.292 g of NH_4VO_3 were separately dissolved in 50 mL of HNO_3 solution with a pH of 0.04, stirred for 30 min until fully dissolved. The two solutions were then combined, followed by the addition of 5 mL of acetonitrile, and stirred for 2 more hours.

Next, Fluorine-doped tin oxide (FTO) glass was cleaned by ultrasonication in acetone, ethanol, and deionized water for 20 min each and dried using nitrogen gas. The glass was placed into the mixed solution with the conductive side facing down, and the BiVO_4 films were grown in a water bath at 65 °C, 75 °C, 85 °C, and 95 °C for 2 h. After the film's growth, the FTO glass was transferred to a muffle furnace, where the temperature was ramped at 10 °C/min to 550 °C, with annealing occurring at this temperature for 2 h. The resulting films were labeled as 65- BiVO_4 , 75- BiVO_4 , 85- BiVO_4 , and 95- BiVO_4 based on the growth temperature.

3. Results and Discussion

The effect of water bath temperature on the crystal growth orientation of BiVO_4 films was systematically investigated. As shown in Figure 1a, BiVO_4 films with tunable crystal orientations were prepared by controlling the water bath temperature during the wet chemical process.

The corresponding top-view and cross-sectional images in Figure 1b–d demonstrate the growth of BiVO_4 crystals on the FTO substrate at different temperatures. At 65°C , BiVO_4 crystals exhibit larger grain sizes and uneven growth (Figure S2). With increasing temperature, crystal density increases, resulting in dense, uniform film thickness of $\sim 5\ \mu\text{m}$. However, the crystal morphology and growth orientation differ across temperatures. At 75°C , BiVO_4 (75-BiVO_4) forms decahedral structures with a 45° angle to the substrate, while at 85°C , BiVO_4 (85-BiVO_4) grows parallel to the substrate with a more regular decahedral shape. In contrast, the 95°C -grown BiVO_4 (95-BiVO_4) exhibits irregular morphology and no distinct growth orientation.

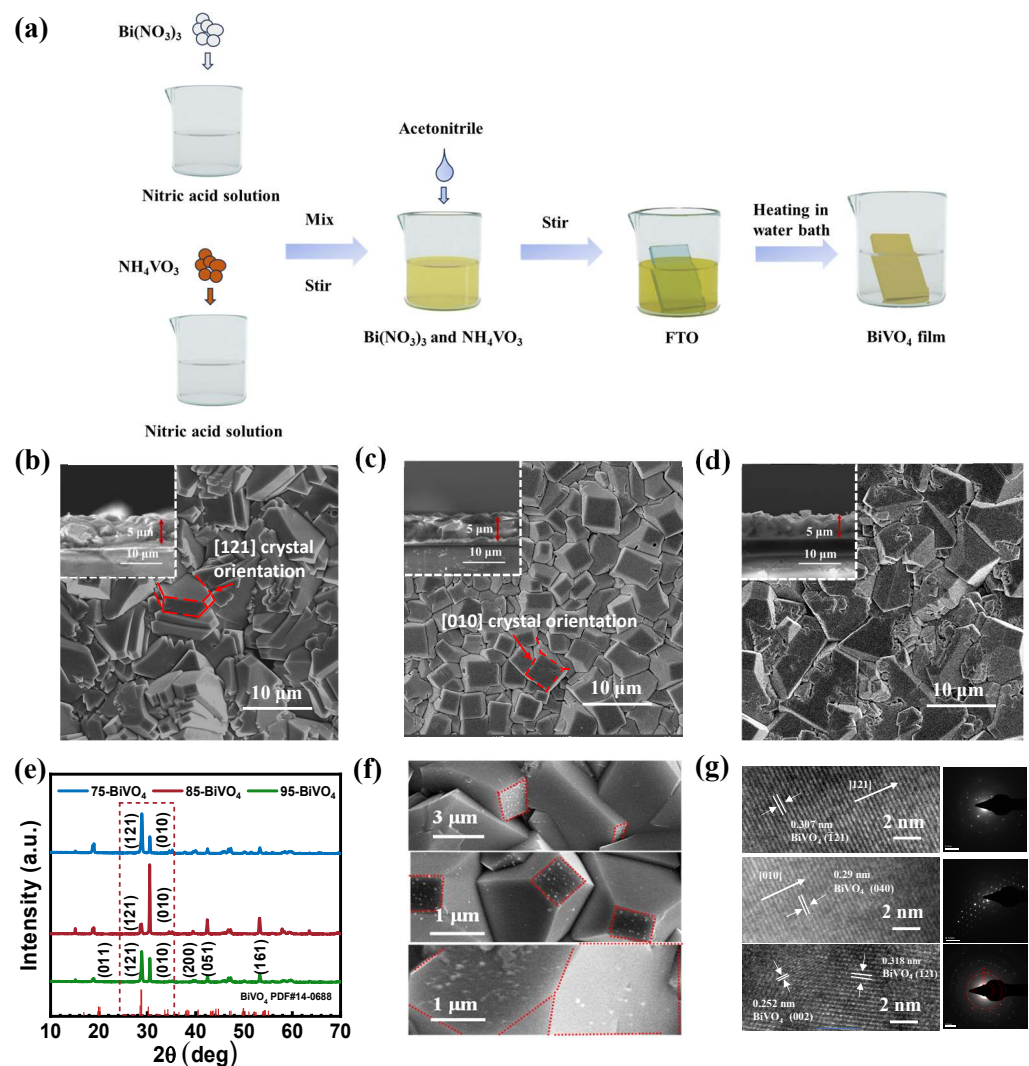


Figure 1. Synthesis and characterizations of BiVO_4 catalytic films: (a) schematic illustration of the synthesis process; (b–d) top-view and cross-sectional SEM images of the BiVO_4 films grown at water bath temperatures of 75°C , 85°C , and 95°C , respectively; (e) XRD patterns; (f) SEM images of Pt photodeposited on BiVO_4 ; (g) HR-TEM images and SAED pattern of typical sample.

To further examine crystal structure and phase composition, X-ray diffraction (XRD) analysis was conducted. Figure 1e shows that all films correspond to monoclinic scheelite-

type BiVO_4 (JCPDS No. 14-0688), with varying diffraction peak intensities [25]. The 75- BiVO_4 film exhibits the strongest (121) facet peak, while the 85- BiVO_4 film shows the highest intensity for the (010) facet. The 95- BiVO_4 film has similar intensities for both the (010) and (121) facets.

In the photodeposition experiment with chloroplatinic acid, due to the electron accumulation on the (010) facet of BiVO_4 , Pt particles preferentially deposit onto the (010) facet [26]. This experimental approach provides a clear basis for determining the exposed crystal facets and crystal growth orientation. As shown in Figure 1f, on the surface of the 75- BiVO_4 film, Pt particles undergo oriented photodeposition along the crystal plane perpendicular to the FTO substrate. In contrast, in 85- BiVO_4 , Pt particles align parallel to the FTO substrate during photodeposition. This phenomenon distinctly reveals the orientation differences between the crystal planes of the 75- BiVO_4 and 85- BiVO_4 films. However, no oriented photodeposition of Pt particles was observed in the 95- BiVO_4 film, indicating an absence of obvious facet exposure. Together with XRD analysis, these findings confirm that the 95- BiVO_4 film lacks a preferred orientation in crystal growth.

As shown in Figure 1g, high-resolution transmission electron microscopy (HR-TEM) images of 75- BiVO_4 and 85- BiVO_4 reveal uniform lattice fringes, and the selected area electron diffraction (SAED) patterns further confirm that the growth directions of these grains are essentially consistent. However, 95- BiVO_4 shows disordered lattice fringes and a ring-like SAED pattern, indicating that the grain growth directions are disordered. Moreover, the evident fringes observed in the high-resolution transmission electron microscopy (HR-TEM) images are basically perpendicular to the longitudinal direction of the nanoparticles. The lattice spacings of 75- BiVO_4 and 85- BiVO_4 are calculated to be 0.307 nm and 0.29 nm, respectively, which match well with the lattice spacings of the (121) and (040) planes of monoclinic BiVO_4 with a space group of $I2/a$. Therefore, combined with XRD and photodeposition tests, it can be confirmed that the nanoparticles of 75- BiVO_4 and 85- BiVO_4 preferentially grow along the [121] and [010] directions, respectively.

Raman and XPS analyses (Figure S3) confirm the purity of the BiVO_4 films, with no significant differences in defects or lattice distortions across different crystal orientations, ensuring that crystal properties aside from orientation remain consistent among the films [27,28].

To explore the intrinsic relationship between BiVO_4 crystal orientation and PEC activity, a series of photoelectrochemical tests were conducted by using the BiVO_4 films as photoanodes in a three-electrode system. First, linear sweep voltammetry (LSV) was performed in 0.5 M Na_2SO_4 electrolyte under AM 1.5 G Xe lamp illumination. As shown in Figure 2a, the [010]-oriented 85- BiVO_4 photoanode achieved a photocurrent density of 0.2 mA cm^{-2} , which is 3.5 times that of [121]-oriented 75- BiVO_4 (0.056 mA cm^{-2}) and double that of the randomly oriented 95- BiVO_4 (0.11 mA cm^{-2}). This highlights the significantly enhanced photocurrent density of the [010]-oriented BiVO_4 photoanode.

Additionally, Figure 2b shows that under identical laser irradiation, the luminescence intensities of the BiVO_4 films vary notably with crystal orientation. The [010]-oriented BiVO_4 shows the lowest luminescence, while the [121]-oriented film exhibits the highest, indicating differences in electron–hole recombination rates [29]. Specifically, the [010]-oriented BiVO_4 has the lowest radiative recombination rate, whereas the [121]-oriented film suffers from the highest recombination.

To further evaluate the wavelength dependence of PEC activity, the incident photon-to-current efficiency (IPCE) of the three films was measured under an applied bias of 1.2 V (vs. RHE) in 0.5 M Na_2SO_4 and 0.1 M Na_2SO_3 solutions [30]. Figure 2c shows that the [010]-oriented 85- BiVO_4 exhibited higher IPCE values, with a rapid drop near 500 nm, consistent with its absorption edge. Even after calculating the absorbed photon-to-current efficiency (APCE) to account for absorption variations, the [010]-oriented BiVO_4 still demonstrated superior PEC performance [31]. These findings indicate that BiVO_4 films grown along the [010] orientation exhibit significantly better PEC activity compared to those grown along other orientations.

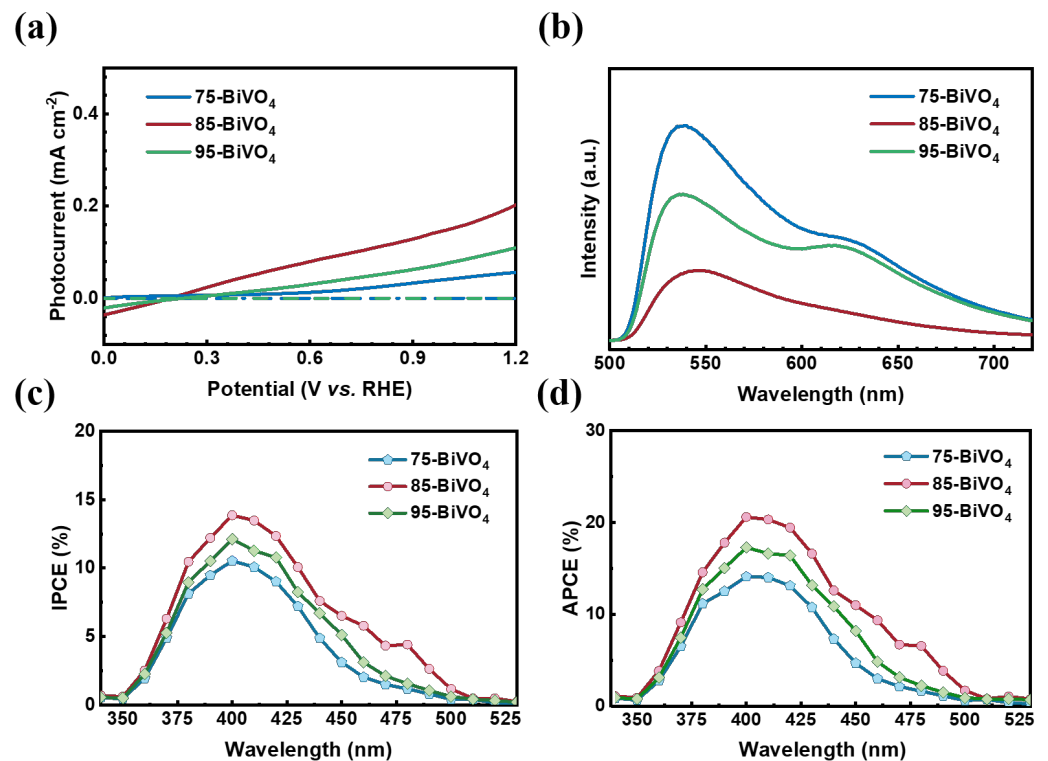


Figure 2. Photoelectrochemical characterization and comparison. (a) I-V curves. (b) PL spectra. (c) IPCE, and (d) APCE of three BiVO₄ films with different crystal orientations.

The photoelectrochemical activity of semiconductors is influenced by three key factors: light absorption rate, carrier separation, and injection efficiencies [32,33]. This study explores the differences in PEC performance of the three BiVO₄ films based on these aspects.

First, the optical properties of the BiVO₄ films were analyzed using UV-vis spectroscopy. As shown in Figure 3a, the light absorption rates of the films with different crystal orientations are similar. All films have an absorption edge at 520 nm, with absorption rates of about 65% for wavelengths shorter than 520 nm and around 20% for longer wavelengths. The optical bandgap, calculated using the Tauc formula (as shown in Equation (1)) [34], is consistently 2.4 eV for all films, indicating minimal impact of crystal orientation on the optical properties.

$$(\alpha h\nu)^{1/n} = A(h\nu - E_g), \quad (1)$$

where α is the absorption coefficient and n is related to the type of transition of the semiconductor. If it is a direct bandgap semiconductor, $n = \frac{1}{2}$, and if it is an indirect bandgap semiconductor, $n = 2$. By drawing the Tauc curve, the intersection point between the slope of the fitted curve and the X-axis is the optical bandgap of the semiconductor. The value of n is $\frac{1}{2}$ because they are all direct bandgap materials of BiVO₄.

Next, the carrier transport characteristics of the BiVO₄ films were investigated using photoelectrochemical testing. By adding 0.1 M Na₂SO₃ as a hole sacrificial agent to the 0.5 M Na₂SO₄ electrolyte, surface recombination of electron-hole pairs was eliminated. The [010]-oriented BiVO₄ film exhibited a photocurrent density of 1.17 mA cm⁻², significantly higher than the other crystal-oriented films. This suggests that crystal orientation affects carrier transport within the films.

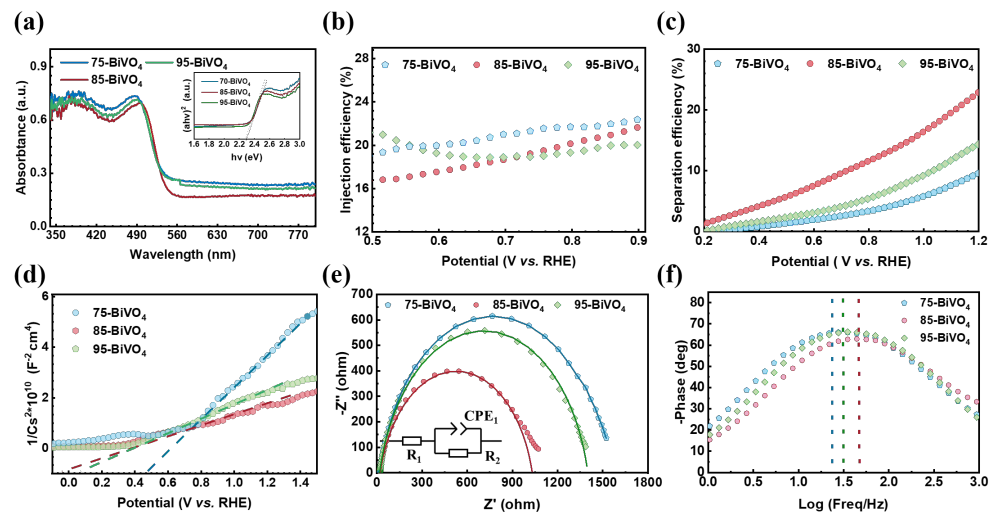


Figure 3. Band structure and photocarrier dynamics analysis. (a) UV-vis absorption spectra, with insets showing optical bandgap widths. (b) Injection efficiency. (c) Separation efficiency. (d) Mott-Schottky curves. (e) EIS. (f) Bode plots.

To assess carrier separation, injection and separation efficiencies were calculated (as shown in Equations (2) and (3)). Figure 3b,c show that while injection efficiency was similar across the three films, the [010]-oriented BiVO_4 exhibited a much higher separation efficiency. This indicates that the superior photocurrent density of the [010]-oriented BiVO_4 is due to more effective carrier separation within the film.

$$\eta_{\text{sep}} = \frac{J_{\text{Na}_2\text{SO}_3}}{J_0}, \quad (2)$$

$$\eta_{\text{inj}} = \frac{J}{J_{\text{Na}_2\text{SO}_3}}, \quad (3)$$

where J is the actual photocurrent density (photocurrent density without sacrificial agent) in the 0.5 M Na_2SO_4 electrolyte, J_0 is the theoretical photocurrent, and $J_{\text{Na}_2\text{SO}_3}$ is the photocurrent density obtained in the 0.5 M Na_2SO_4 electrolyte with 0.1 M Na_2SO_3 .

Further insights were gained from Mott-Schottky tests, which confirmed that all BiVO_4 films are n-type semiconductors, regardless of their crystal orientation [35]. The carrier concentration of the [010]-oriented BiVO_4 was $1.087 \times 10^{18} \text{ cm}^{-3}$, significantly higher than that of the 75- BiVO_4 and 95- BiVO_4 films. This confirms that fewer electron-hole pairs recombine in the [010]-oriented film, leading to higher carrier availability at the surface and superior photocurrent density.

Finally, electrochemical impedance spectroscopy (EIS) was used to examine carrier transport dynamics [36]. In this experiment, measurements were conducted under illumination. A constant voltage of 0.61 V (vs. RHE) was applied, with a frequency range of 0.1 Hz to 1000 kHz, an AC amplitude of 10 mV (vs. Ag/AgCl), and saturated Na_2SO_4 (0.5 M) solution as the electrolyte. The [010]-oriented BiVO_4 film exhibited the lowest resistance and the shortest carrier lifetime (2.99 ms), demonstrating that carriers can be injected into the electrolyte more quickly, as shown in the Bode plot. These results demonstrate that this film has superior carrier transport properties, leading to enhanced separation efficiency, photocurrent density, and photoelectric conversion efficiency.

Kelvin probe microscope (KPFM) was employed to explore the surface morphology and surface potential distribution of individual BiVO_4 crystal particles more intuitively [37–39]. As shown in Figure 4a,d,g, the morphological characteristics of monoclinic BiVO_4 films with different crystal orientations are consistent with the SEM observations. These images clearly

demonstrate the distinct surface features of the BiVO_4 particles, which vary depending on the crystal orientation.

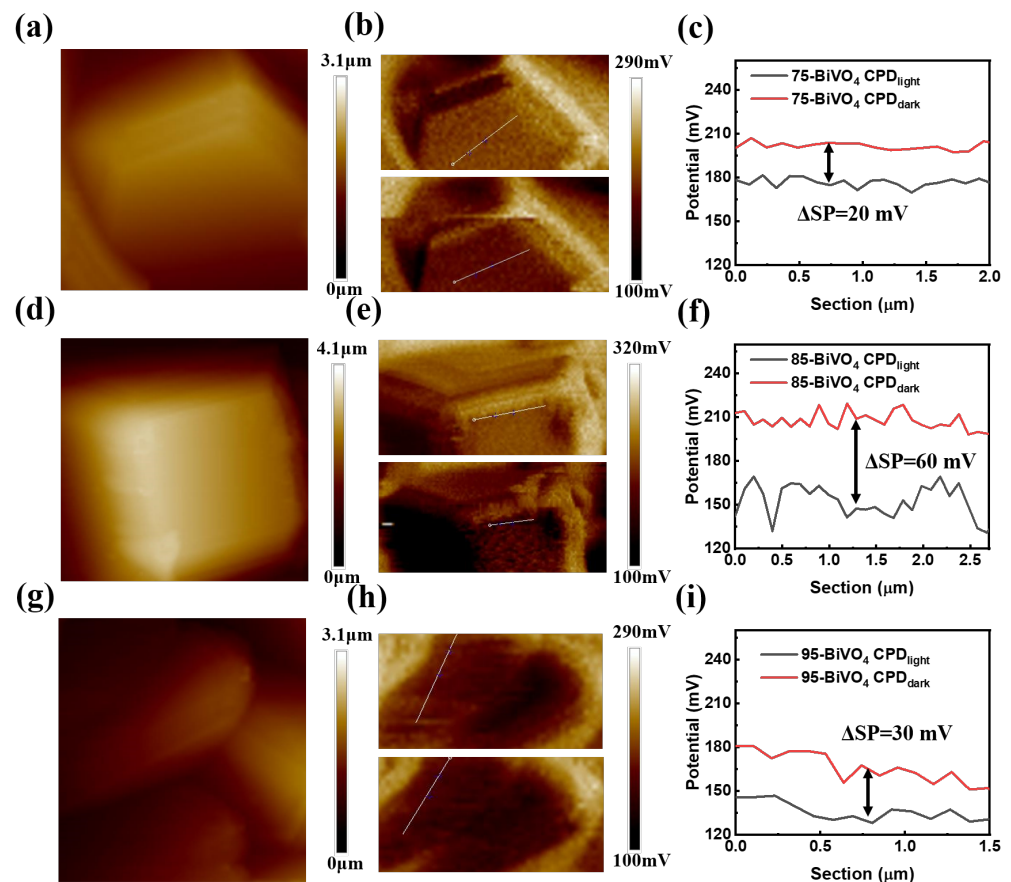


Figure 4. Surface potential measurements with KPFM. (a,d,g) Surface morphology images of 75-BiVO₄, 85-BiVO₄, and 95-BiVO₄, respectively. (b,e,h) Surface potential mappings for the same samples, with the top row showing measurements in the dark and the bottom row showing measurements under UV illumination. (c,f,i) Surface potential distributions along the marked line in the corresponding surface potential images (b,e,h).

The influence of UV illumination on surface potential was also investigated, revealing important insights into carrier dynamics. As shown in Figure 4b,e,h, surface potential mappings under UV illumination (bottom images) exhibit a significant decrease compared to the dark conditions (top images). This reduction occurs because, when exposed to UV light, the Pt-coated probe with a higher work function causes photogenerated electrons to accumulate within the bulk of the BiVO_4 particles, while photogenerated holes migrate to the surface. This shift results in a more positive surface potential for n-type semiconductors, reducing the measured contact potential difference (CPD) [40].

The extent of this surface potential change is closely related to carrier separation efficiency. As shown in Figure 4c,f,i, the surface potential difference (ΔSP) for 85-BiVO₄ particles is 60 mV, significantly higher than the ΔSP values for 75-BiVO₄ (20 mV) and 95-BiVO₄ (30 mV). This suggests that the 85-BiVO₄ crystal particles experience greater changes in surface Fermi level under illumination, indicating more effective separation of photogenerated carriers. As a result, more carriers reach the surface, leading to reduced carrier recombination within the 85-BiVO₄ particles.

This enhanced carrier separation in 85-BiVO₄ provides a clear explanation for its superior photoelectric performance, which is consistent with the earlier findings. These results further underscore the importance of crystal orientation in optimizing the photoelectrochemical properties of BiVO_4 films.

To assess the influence of BiVO₄ crystal growth orientation on internal carrier transport resistance, carrier mobility within BiVO₄ crystal particles of varying orientations was measured using conductive atomic force microscopy (C-AFM). As shown in Figure 5, a high-work-function Pt-Ir coated probe was used as a movable nanoscale electrical contact point. When the probe contacts BiVO₄ crystal particles, the difference in work functions results in a barrier. This allows for the application of the space-charge-limited current (SCLC) model to quantify carrier mobility in BiVO₄. C-AFM offers high-resolution local I-V curve measurements with the added benefit of eliminating pinhole effects, providing valuable insights into carrier mobility. However, the geometry of the probe tip inevitably influences test results [41]. To account for this, the Johnson–Kendall–Roberts (JKR) contact model was employed to calculate the carrier mobility within different BiVO₄ crystal particles [42,43]:

$$J = \alpha \epsilon \epsilon_0 \mu \frac{(V - V_{bi})^2}{L^3} \left(\frac{L}{d}\right)^{1.6}, \quad (4)$$

Here, J is the photocurrent density. α is a prefactor determined by Reid et al. through finite element modeling, with a value of 8.2, replacing the $\frac{9}{8}$ factor used in the Mott–Gurney law for planar electrodes. This adjustment eliminates errors caused by the non-uniform electric field at the probe tip. In this equation, ϵ is the relative dielectric constant of the film, ϵ_0 is the vacuum dielectric constant, μ is the carrier mobility, V is the applied voltage, and V_{bi} is the built-in potential caused by the work function difference between the contact electrodes. L is the film thickness. To account for the probe tip shape, the factor $\left(\frac{L}{d}\right)^{1.6}$ is introduced, further reducing errors due to the curvature of the tip. Specific parameters can be found in Table S2.

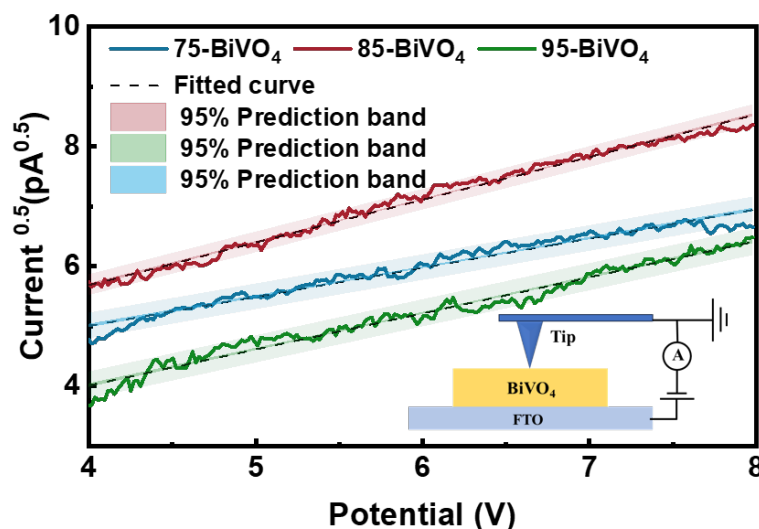


Figure 5. Local I-V curves measured with C-AFM.

Using Equation (4), the carrier mobility of the three BiVO₄ photoanodes was calculated. The 85-BiVO₄ shows a carrier mobility of $7.647 \times 10^{-3} \text{ cm}^2 \text{ V}^{-1} \text{ s}^{-1}$, which is significantly higher than that of 75-BiVO₄ ($3.572 \times 10^{-3} \text{ cm}^2 \text{ V}^{-1} \text{ s}^{-1}$) and 95-BiVO₄ ($4.988 \times 10^{-3} \text{ cm}^2 \text{ V}^{-1} \text{ s}^{-1}$). This increased carrier mobility in 85-BiVO₄ indicates more efficient photogenerated charge transport, contributing to its superior PEC performance, especially along the [010] crystal orientation.

4. Conclusions

In conclusion, this study successfully fabricated BiVO₄ films with distinct crystal orientations via a wet chemical method and systematically investigated their photoelectrochemical properties. The films grown along the [010] crystal orientation demonstrated notably superior PEC performance, which can be attributed to reduced carrier recomb-

nation and enhanced charge separation efficiency. Surface potential measurements and conductive atomic force microscopy revealed that the [010]-oriented BiVO₄ films possess higher carrier mobility, leading to lower internal transport resistance and more efficient charge transport to the surface. This enhanced mobility was confirmed to play a pivotal role in the observed improvements in PEC activity. Furthermore, this study highlights the critical role of crystal facet engineering in optimizing semiconductor performance for PEC applications. By orienting crystal growth along specific facets, such as [010], it is possible to increase carrier mobility and improve overall photocatalytic efficiency. These findings provide valuable insights for developing advanced photoelectrodes with higher carrier transport efficiency, paving the way for more effective solar energy conversion and environmental remediation technologies. Further research could explore the effects of other crystal orientations and multi-faceted BiVO₄ structures, potentially leading to even more efficient photoanodes for solar energy conversion. Additionally, combining this strategy with other co-catalysts or hybrid materials could significantly boost PEC performance for practical applications.

Supplementary Materials: The following supporting information can be downloaded at: <https://www.mdpi.com/article/10.3390/nano14231870/s1>, the instruments and their corresponding models used in this paper, the specific testing parameters, the formulas used for calculations, and some supplementary data. Figure S1: Top-view SEM images of BiVO₄ films grown for different durations in a water bath at 85 °C. Figure S2: SEM top-view images (a) and (b), as well as a cross-sectional view (c) of BiVO₄ films grown in a water bath at 65 °C. Figure S3: Raman spectra (a) and XPS survey spectra (b) of the three films. Figure S4: (a) The I-t analysis of the BiVO₄ films under light on/off cycles and (b) the stability test of the BiVO₄ films under continuous illumination. Figure S5: XRD images of (a) 75-BiVO₄, (b) 85-BiVO₄, and (c) 95-BiVO₄ photoanodes before and after stability testing. Figure S6: SEM images of (a) 75-BiVO₄, (c) 85-BiVO₄, and (e) 95-BiVO₄ photoanodes before stability testing, along with SEM images of (b) 75-BiVO₄, (d) 85-BiVO₄, and (f) 95-BiVO₄ photoanodes after stability testing. Figure S7: Electrochemical active surface area (ECSA) measurements, including cyclic voltammetry (C-V) curves of (a) 75-BiVO₄, (b) 85-BiVO₄, and (c) 95-BiVO₄ photoanodes, as well as (d) the plots of capacitive current to scan rate. Figure S8: I-V characteristics measured in a mixed electrolyte of 0.5 M Na₂SO₄ and 0.1 M Na₂SO₃ under (a) illuminated and (b) dark conditions. Figure S9: Local I-V curves measured by conductive atomic force microscopy (C-AFM). Table S1: Summary of the slope and carrier concentrations. Table S2: Carrier mobility determined from the local I-V curves. Table S3: The fitting results of EIS Nyquist spectra.

Author Contributions: H.Z.: conceptualization, data curation, methodology, formal analysis, visualization, and writing—original draft; X.W.: conceptualization, investigation, validation, and project administration; Y.P.: conceptualization, investigation, and writing—review and editing; W.H.: conceptualization, resources, project administration, supervision, funding acquisition, and writing—review and editing. All authors have read and agreed to the published version of the manuscript.

Funding: This research received no external funding.

Data Availability Statement: The original contributions presented in the study are included in this article; further inquiries can be directed to the corresponding author.

Conflicts of Interest: The authors declare no conflicts of interest.

References

1. Zhang, J. Metal oxide nanomaterials for solar hydrogen generation from photoelectrochemical water splitting. *MRS Bull.* **2011**, *36*, 48–55. [[CrossRef](#)]
2. He, H.; Liao, A.; Guo, W.; Luo, W.; Zhou, Y.; Zou, Z. State-of-the-art progress in the use of ternary metal oxides as photoelectrode materials for water splitting and organic synthesis. *Nano Today* **2019**, *28*, 100763. [[CrossRef](#)]
3. Chen, Y.; Feng, X.; Liu, Y.; Guan, X.; Burda, C.; Guo, L. Metal Oxide-Based Tandem Cells for Self-Biased Photoelectrochemical Water Splitting. *ACS Energy Lett.* **2020**, *5*, 844–866. [[CrossRef](#)]
4. Yang, Y.; Niu, S.; Han, D.; Liu, T.; Wang, G.; Li, Y. Progress in Developing Metal Oxide Nanomaterials for Photoelectrochemical Water Splitting. *Adv. Energy Mater.* **2017**, *7*, 1700555. [[CrossRef](#)]

5. Chen, W.; Liu, S.; Fu, Y.; Yan, H.; Qin, L.; Lai, C.; Zhang, C.; Ye, H.; Chen, W.; Qin, F.; et al. Recent advances in photoelectrocatalysis for environmental applications: Sensing, pollutants removal and microbial inactivation. *Coord. Chem. Rev.* **2022**, *454*, 214341. [[CrossRef](#)]
6. Lianos, P. Review of recent trends in photoelectrocatalytic conversion of solar energy to electricity and hydrogen. *Appl. Catal. B Environ.* **2017**, *210*, 235–254. [[CrossRef](#)]
7. Chatterjee, P.; Ambati, M.; Chakraborty, A.; Chakraborty, S.; Biring, S.; Ramakrishna, S.; Wong, T.; Kumar, A.; Lawaniya, R.; Dalapati, G. Photovoltaic/photo-electrocatalysis integration for green hydrogen: A review. *Energy Convers. Manag.* **2022**, *261*, 115648. [[CrossRef](#)]
8. Zhong, S.; Xi, Y.; Wu, S.; Liu, Q.; Zhao, L.; Bai, S. Hybrid cocatalysts in semiconductor-based photocatalysis and photoelectrocatalysis. *J. Mater. Chem. A* **2020**, *8*, 14863–14894. [[CrossRef](#)]
9. Tamirat, A.; Rick, J.; Dubale, A.; Su, W.N.; Hwang, B.J. Using hematite for photoelectrochemical water splitting: A review of current progress and challenges. *Nanoscale Horiz.* **2016**, *1*, 243–267. [[CrossRef](#)]
10. Nair, V.; Perkins, C.; Lin, Q.; Law, M. Textured nanoporous Mo:BiVO₄ photoanodes with high charge transport and charge transfer quantum efficiencies for oxygen evolution. *Energy Environ. Sci.* **2016**, *9*, 1412–1429. [[CrossRef](#)]
11. Peng, Q.; Kalanyan, B.; Hoertz, P.; Miller, A.; Kim, D.; Hanson, K.; Alibabaei, L.; Liu, J.; Meyer, T.; Parsons, G.; et al. Solution-Processed, Antimony-Doped Tin Oxide Colloid Films Enable High-Performance TiO₂ Photoanodes for Water Splitting. *Nano Lett.* **2013**, *13*, 1481–1488. [[CrossRef](#)] [[PubMed](#)]
12. Song, J.; Seo, M.; Lee, T.; Jo, Y.R.; Lee, J.; Kim, T.; Kim, S.Y.; Kim, S.M.; Jeong, S.; An, H.; et al. Tailoring Crystallographic Orientations to Substantially Enhance Charge Separation Efficiency in Anisotropic BiVO₄ Photoanodes. *ACS Catal.* **2018**, *8*, 5952–5962. [[CrossRef](#)]
13. Niu, W.; Moehl, T.; Adams, P.; Zhang, X.; Lefèvre, R.; Cruz, A.; Zeng, P.; Kunze, K.; Yang, W.; Tilley, S. Crystal orientation-dependent etching and trapping in thermally-oxidised Cu₂O photocathodes for water splitting. *Energy Environ. Sci.* **2022**, *15*, 2002–2010. [[CrossRef](#)]
14. Kment, S.; Schmuki, P.; Hubicka, Z.; Machala, L.; Kirchgeorg, R.; Liu, N.; Wang, L.; Lee, K.; Olejnicek, J.; Cada, M.; et al. Photoanodes with Fully Controllable Texture: The Enhanced Water Splitting Efficiency of Thin Hematite Films Exhibiting Solely (110) Crystal Orientation. *ACS Nano* **2015**, *9*, 7113–7123. [[CrossRef](#)] [[PubMed](#)]
15. Pan, L.; Dai, L.; Burton, O.; Chen, L.; Andrei, V.; Zhang, Y.; Ren, D.; Cheng, J.; Wu, L.; Frohna, K.; et al. High carrier mobility along the [111] orientation in Cu₂O photoelectrodes. *Nature* **2024**, *628*, 765–770. [[CrossRef](#)] [[PubMed](#)]
16. Kay, A.; Cesar, I.; Grätzel, M. New Benchmark for Water Photooxidation by Nanostructured α -Fe₂O₃ Films. *J. Am. Chem. Soc.* **2006**, *128*, 15714–15721. [[CrossRef](#)]
17. Lin, R.; Wan, J.; Xiong, Y.; Wu, K.; Cheong, W.; Zhou, G.; Wang, D.; Peng, Q.; Chen, C.; Li, Y. Quantitative Study of Charge Carrier Dynamics in Well-Defined WO₃ Nanowires and Nanosheets: Insight into the Crystal Facet Effect in Photocatalysis. *J. Am. Chem. Soc.* **2018**, *140*, 9078–9082. [[CrossRef](#)]
18. Kim, C.; Yeob, S.; Cheng, H.M.; Kang, Y. A selectively exposed crystal facet-engineered TiO₂ thin film photoanode for the higher performance of the photoelectrochemical water splitting reaction. *Energy Environ. Sci.* **2015**, *8*, 3646–3653. [[CrossRef](#)]
19. Yang, M.; Fan, Z.; Du, J.; Li, R.; Liu, D.; Zhang, B.; Feng, K.; Feng, C.; Li, Y. Tailoring the Crystallographic Orientation of a Sb₂S₃ Thin Film for Efficient Photoelectrochemical Water Reduction. *ACS Catal.* **2022**, *12*, 8175–8184. [[CrossRef](#)]
20. Wang, S.; Liu, G.; Wang, L. Crystal Facet Engineering of Photoelectrodes for Photoelectrochemical Water Splitting. *Chem. Rev.* **2019**, *119*, 5192–5247. [[CrossRef](#)]
21. Lu, Y.; Yang, Y.; Fan, X.; Li, Y.; Zhou, D.; Cai, B.; Wang, L.; Fan, K.; Zhang, K. Boosting Charge Transport in BiVO₄ Photoanode for Solar Water Oxidation. *Adv. Mater.* **2022**, *34*, 2108178. [[CrossRef](#)] [[PubMed](#)]
22. Wang, S.; Chen, P.; Bai, Y.; Yun, J.H.; Liu, G.; Wang, L. New BiVO₄ Dual Photoanodes with Enriched Oxygen Vacancies for Efficient Solar-Driven Water Splitting. *Adv. Mater.* **2018**, *30*, 1800486. [[CrossRef](#)] [[PubMed](#)]
23. Zhong, D.; Choi, S.; Gamelin, D. Near-Complete Suppression of Surface Recombination in Solar Photoelectrolysis by “Co-Pi” Catalyst-Modified W:BiVO₄. *J. Am. Chem. Soc.* **2011**, *133*, 18370–18377. [[CrossRef](#)] [[PubMed](#)]
24. Kim, J.; Lee, J. Elaborately Modified BiVO₄ Photoanodes for Solar Water Splitting. *Adv. Mater.* **2019**, *31*, 1806938. [[CrossRef](#)]
25. Li, D.; Liu, Y.; Shi, W.; Shao, C.; Wang, S.; Ding, C.; Liu, T.; Fan, F.; Shi, J.; Li, C. Crystallographic-Orientation-Dependent Charge Separation of BiVO₄ for Solar Water Oxidation. *ACS Energy Lett.* **2019**, *4*, 825–831. [[CrossRef](#)]
26. Li, R.; Zhang, F.; Wang, D.; Yang, J.; Li, M.; Zhu, J.; Zhou, X.; Han, H.; Li, C. Spatial separation of photogenerated electrons and holes among {010} and {110} crystal facets of BiVO₄. *Nat. Commun.* **2013**, *4*, 1432. [[CrossRef](#)]
27. Ureña-Begara, F.; Crunteanu, A.; Raskin, J.P. Raman and XPS Characterization of Vanadium Oxide Thin Films with Temperature. *Appl. Surf. Sci.* **2017**, *403*, 717–727. [[CrossRef](#)]
28. Christian, H. New Advances in Using Raman Spectroscopy for the Characterization of Catalysts and Catalytic Reactions. *Chem. Soc. Rev.* **2021**, *50*, 3519–3564. [[CrossRef](#)]
29. Moniz, S.; Zhu, J.; Tang, J. 1D Co-Pi Modified BiVO₄/ZnO Junction Cascade for Efficient Photoelectrochemical Water Cleavage. *Adv. Energy Mater.* **2014**, *4*, 1301590. [[CrossRef](#)]
30. Yang, J.; Park, I.; Lee, S.; Lee, M.; Lee, T.; Park, H.; Kim, C.; Park, J.; Moon, J.; Kim, J.; et al. Near-Complete Charge Separation in Tailored BiVO₄-Based Heterostructure Photoanodes Toward Artificial Leaf. *Appl. Catal. B Environ.* **2021**, *293*, 120217. [[CrossRef](#)]

31. Hisatomi, T.; Kubota, J.; Domen, K. Recent Advances in Semiconductors for Photocatalytic and Photoelectrochemical Water Splitting. *Chem. Soc. Rev.* **2014**, *43*, 7520–7535. [[CrossRef](#)] [[PubMed](#)]
32. Sivula, K.; van de Krol, R. Semiconducting Materials for Photoelectrochemical Energy Conversion. *Nat. Rev. Mater.* **2016**, *1*, 15010. [[CrossRef](#)]
33. Kumar, S.; Ahirwar, S.; Satpati, A. Insight into the PEC and Interfacial Charge Transfer Kinetics at the Mo Doped BiVO₄ Photoanodes. *RSC Adv.* **2019**, *9*, 41368–41382. [[CrossRef](#)] [[PubMed](#)]
34. Roy, D.; Samu, G.; Hossain, M.; Janáky, C.; Rajeshwar, K. On the measured optical bandgap values of inorganic oxide semiconductors for solar fuels generation. *Catal. Today* **2018**, *300*, 136–144. [[CrossRef](#)]
35. Tayyebi, A.; Soltani, T.; Lee, B.K. Effect of pH on Photocatalytic and Photoelectrochemical (PEC) Properties of Monoclinic Bismuth Vanadate. *J. Colloid Interface Sci.* **2019**, *534*, 37–46. [[CrossRef](#)]
36. Tayebi, M.; Kolaei, M.; Tayyebi, A.; Masoumi, Z.; Belbasi, Z.; Lee, B.K. Reduced Graphene Oxide (RGO) on TiO₂ for an Improved Photoelectrochemical (PEC) and Photocatalytic Activity. *Sol. Energy* **2019**, *190*, 185–194. [[CrossRef](#)]
37. Zhang, S.; Xing, Z.; Ma, M.; Liu, Z.; Tang, W.; Kim, S.; Wu, R.; Li, J.; Park, J. Interfacial Nitrogen Modulated Z-scheme Photoanode for Solar Water Oxidation. *J. Power Sources* **2022**, *519*, 230784. [[CrossRef](#)]
38. Ma, M.; Xing, Z.; Zhu, X.; Jiang, P.; Wang, X.; Lin, H.; An, Y.; Su, H.; Yang, S. Interface Modulation of BiVO₄ Based Photoanode with Bi(III)Bi(V)O₄ for Enhanced Solar Water Splitting. *J. Catal.* **2020**, *391*, 513–521. [[CrossRef](#)]
39. Yang, L.; Xiong, Y.; Xiao, P.; Zhang, Y. Guiding Charge Transfer Kinetics into Cocatalyst for Efficient Solar Water Splitting. *Electrochim. Acta* **2019**, *307*, 43–50. [[CrossRef](#)]
40. Hu, Y.; Jin, Y.; Gao, Y.; Li, M.; Wang, X.; Ma, H.; Zhang, Y. Interface and Defect Engineering in 3D Co₃O₄-Ov/TiO₂ to Boost Simultaneous Removal of BPA and Cr(VI) upon Photoelectrocatalytic/Peroxymonosulfate (PEC/PMS) System. *Adv. Funct. Mater.* **2024**, 2414350. [[CrossRef](#)]
41. Button, S.; Mativetsky, J. High-Resolution Charge Carrier Mobility Mapping of Heterogeneous Organic Semiconductors. *Appl. Phys. Lett.* **2017**, *111*, 083302. [[CrossRef](#)]
42. Reid, O.; Munechika, K.; Ginger, D. Space Charge Limited Current Measurements on Conjugated Polymer Films Using Conductive Atomic Force Microscopy. *Nano Lett.* **2008**, *8*, 1602–1609. [[CrossRef](#)] [[PubMed](#)]
43. Goh, C.; Kline, R.; McGehee, M.; Kadnikova, E.; Fréchet, J. Molecular-Weight-Dependent Mobilities in Regioregular Poly(3-Hexyl-Thiophene) Diodes. *Appl. Phys. Lett.* **2005**, *86*, 122110. [[CrossRef](#)]

Disclaimer/Publisher's Note: The statements, opinions and data contained in all publications are solely those of the individual author(s) and contributor(s) and not of MDPI and/or the editor(s). MDPI and/or the editor(s) disclaim responsibility for any injury to people or property resulting from any ideas, methods, instructions or products referred to in the content.